

promoting access to White Rose research papers



Universities of Leeds, Sheffield and York
<http://eprints.whiterose.ac.uk/>

This is an author produced version of a paper published in **IEEE Transactions on Ultrasonics, Ferroelectrics and Frequency Control**.

White Rose Research Online URL for this paper:

<http://eprints.whiterose.ac.uk/77074/>

Paper:

Harput, S, Arif, M, McLaughlan,, J, Cowell, DMJ and Freear, S (2013) *The Effect of Amplitude Modulation on Subharmonic Imaging with Chirp Excitation*. IEEE Transactions on Ultrasonics, Ferroelectrics and Frequency Control, 60 (12). 2532.

<http://dx.doi.org/10.1109/TUFFC.2013.2852>

The Effect of Amplitude Modulation on Subharmonic Imaging with Chirp Excitation

Sevan Harput, Muhammad Arif, James McLaughlan, David M. J. Cowell, and Steven Freear, *Senior Member, IEEE*

Abstract—Subharmonic generation from ultrasound contrast agents depends on the spectral and temporal properties of the excitation signal. The subharmonic response can be improved by using wideband and long duration signals. However, for sinusoidal tone-burst excitation the effective bandwidth of the signal is inversely proportional with the signal duration. Linear frequency modulated (LFM) and nonlinear frequency modulated (NLFM) chirp excitations allow independent control over the signal bandwidth and duration, therefore in this study LFM and NLFM signals were used for the insonation of microbubble populations. The amplitude modulation of the excitation waveform was achieved by applying different window functions. A customized window was designed for the NLFM chirp excitation by focusing on reducing the spectral leakage at the subharmonic frequency and increasing the subharmonic generation from microbubbles.

Subharmonic scattering from a microbubble population was measured for various excitation signals and window functions. At a peak-negative pressure of 600 kPa, the generated subharmonic energy by ultrasound contrast agents was 15.4 dB more for NLFM chirp excitation with 40% fractional bandwidth when compared to tone-burst excitation. For this reason, the NLFM chirp with a customized window was used as an excitation signal to perform subharmonic imaging in an ultrasound flow phantom. Results showed that the NLFM waveform with a customized window improved the subharmonic contrast by 4.35 ± 0.42 dB on average over a Hann windowed LFM excitation.

Index Terms—Subharmonic imaging, coded excitation, chirps, nonlinear frequency modulation, amplitude modulation, window function, ultrasound contrast agents, microbubbles.

I. INTRODUCTION

ULTRASOUND harmonic imaging offers the potential to improve the contrast-to-tissue ratio (CTR) as microbubbles present in the blood have unique acoustic signatures. At low acoustic pressures (< 100 kPa), ultrasound contrast agents (UCAs) are able to emit energy at the fundamental, second harmonic, subharmonic and ultra-harmonic frequencies. These nonlinear harmonic components are exploited in ultrasound contrast imaging to enhance the contrast between the blood and surrounding tissue [1]. Some of these techniques are commercially available such as harmonic imaging [2], pulse inversion [3] and power modulation [4].

Contrast harmonic imaging based on the second harmonic emission from microbubbles improves CTR as well as the

spatial resolution, since the bandwidth of the second harmonic component is twice the fundamental frequency of the excitation signal [5]. Second harmonic imaging provides an improvement in the CTR because of the weak nonlinear response of tissue over UCAs, especially for low acoustic pressure ranges [6]. Most medical ultrasound imaging systems offer second harmonic imaging to improve the spatial resolution and it is widely used in clinical applications [7]. However, generation of the second harmonic component due to the nonlinear propagation of ultrasound waves through tissue can degrade the contrast of the image at diagnostic pressure levels [8].

The main advantage of subharmonic imaging over second harmonic imaging is the potential to suppress linear and nonlinear tissue echoes [9]–[11]. Imaging at the subharmonic frequency can maximize the CTR as it is solely generated by microbubbles [6]. Another advantage of subharmonic imaging with respect to the harmonic imaging technique is the lower tissue attenuation. Second harmonic will be attenuated more because of the frequency-dependent attenuation in tissue. However, the lower frequency subharmonic component will experience less attenuation as it propagates; resulting in an improved penetration depth [9], [11]. Therefore, the generation of the subharmonic oscillations from UCAs is favorable in many applications such as; subharmonic imaging [9], [12], noninvasive blood pressure estimation [13]–[15], intravascular contrast imaging [16], molecular imaging [17], three-dimensional ultrasound imaging [18]. For this reason, many detection methods have been proposed based on novel excitation techniques to enhance the subharmonic emission from microbubbles [19]–[23].

The main limitation of subharmonic imaging is that the bandwidth of the subharmonic component is half of the excitation bandwidth, which results in a reduction in the axial resolution. However, the degraded resolution does not have a crucial effect on the final outcome, since it is common to display the subharmonic images and the fundamental B-mode images simultaneously [12]. Therefore, in this study the subharmonic data is overlaid with the fundamental data to create a *composite image*, which have the CTR of a subharmonic image and the resolution of a fundamental image.

A. Maximizing the Subharmonic Generation from UCAs

It is believed that asymmetric bubble oscillations are responsible for subharmonic emissions from UCAs. The ideas of *compression-only* and *expansion-dominated* behaviors of

Sevan Harput, James McLaughlan, David M. J. Cowell and Steven Freear are with the Ultrasound Group, School of Electronic and Electrical Engineering, University of Leeds, Leeds, LS2 9JT, UK. (E-mail: s.harput@leeds.ac.uk, s.freear@leeds.ac.uk)

Muhammad Arif is with the Department of Biomedical Engineering, Mehran University of Engineering & Technology, Jamshoro, Pakistan.

microbubbles are widely supported as being the main reason for subharmonic generation from phospholipid coated microbubbles [24]–[26]. Even though the dynamics of subharmonic oscillations are not completely understood, it has been demonstrated that the subharmonic generation of the microbubbles depends on the excitation pressure, waveform, and frequency.

The pressure threshold for subharmonic generation is minimized when the insonation frequency is twice the resonance frequency of the microbubbles [27]. This scheme allows the optimum energy transfer between the forced oscillation and the natural oscillation of microbubbles. Beside the pressure dependency, the subharmonic component is strongly affected by the temporal properties of the excitation waveform [19], [20]. The subharmonic components can be generated more efficiently by increasing the duration of acoustic emissions above certain thresholds, however long duration sinusoidal signals are not suitable for imaging applications [10]. To solve this problem, a chirp coded excitation method can be used and the axial resolution can be recovered by applying pulse compression on the received waveform [20].

Shekhar and Doyle used a chirp waveform to increase the nonlinear microbubble oscillations by spreading the excitation energy across a wider frequency range and achieved stronger subharmonic oscillations at lower pressure thresholds [28]. They showed the effect of tapering on subharmonic emission from microbubbles and employed a long duration wideband excitation with a rectangular window for subharmonic intravascular ultrasound imaging to improve the sensitivity. Daeichin *et al.* also preferred a rectangular envelope to maximize the subharmonic emission from microbubbles [29].

These previous studies suggest that wideband, long duration, and rectangular windowed waveforms will maximize the subharmonic generation. However the rectangular window is not desirable for imaging applications because of the spectral leakage, where the transmitted signal's energy is not confined at the desired frequency band, but spread to a wider frequency range. The energy leakage from the fundamental frequency component to the other frequencies will increase the scattering from tissue at the subharmonic frequency, which will reduce the achievable CTR of the subharmonic image.

The aim of this study was to analyze the effect of amplitude modulation on excitation signal for subharmonic imaging with chirps. The amplitude modulation of a linear frequency modulated (LFM) chirp was controlled by applying a window function. The amplitude modulation of a nonlinear frequency modulated (NLFM) chirp was controlled by its tangential instantaneous frequency function, which gives more flexibility on waveform design. Different window functions were compared and benchmarked according to their capability of generating subharmonic emissions from microbubbles while minimizing the spectral leakage. The performance of a Hann windowed LFM and a custom windowed NLFM chirp excitations were experimentally investigated and the results were compared for subharmonic imaging.

II. CODED EXCITATION: THEORY AND SIGNAL DESIGN

In conventional pulsed excitation, the required penetration depth can be achieved by increasing either the peak acoustic pressure or the signal duration. Increasing the peak acoustic pressure can be harmful for the human body, where limitations on peak negative pressure are set by the food and drug administration (FDA) in order to prevent inertial cavitation and tissue damage [30]. Increasing the signal duration will reduce the signal bandwidth and hence the axial resolution.

Coded excitation techniques were originally introduced in radar communication systems in the 1950s and have shown great potential to provide improved SNR [31]. These coding techniques are now also well known in medical imaging and have been applied to clinical ultrasound systems to improve the SNR and penetration depth without increasing the peak acoustic pressure [32], [33]. In ultrasound systems with coded excitation, the signal coding schemes are based on either frequency modulation or phase modulation. Signals based on phase modulation are binary coded sequences which uses sinusoidal bursts of one to several cycles with alternating phases of 0° and 180° . The most practical binary code in ultrasound imaging system is the Golay sequence. Implementation of a binary coding scheme in ultrasound contrast imaging is very challenging as the phase of the transmitted signal is not preserved due to the nonlinear scattering from microbubbles [34], [35]. Also it requires multiple transmissions which degrades the system frame-rate and may cause poor cancellation of range sidelobes under tissue motion. The coded signals based on frequency modulation are referred to as chirps and their frequency change linearly or nonlinearly over time. Chirps are more robust to the distortion caused by the frequency dependent attenuation as the ultrasound wave propagates through the soft tissue [36].

The transmission of long duration chirps will increase the total energy of the system, which will result in an SNR gain of time-bandwidth-product of the signal. On the receiving side bandwidth plays an important role on the axial resolution, which is recovered by reducing the initial duration of the chirp signal using a matched filter. After pulse compression the axial resolution of the compressed chirp signal is comparable to a conventional un-modulated pulse of the same bandwidth.

A. Linear Frequency Modulated (LFM) Signals

A LFM signal, $x(t)$, can be expressed in analytical form as

$$\begin{aligned} x(t) &= p(t) e^{j2\pi\phi(t)}, \quad 0 \leq t \leq T \\ x(t) &= 0, \quad \text{else} \end{aligned} \quad (1)$$

where $p(t)$ and $\phi(t)$ are the amplitude modulation and phase modulation functions respectively. The phase modulation function of the LFM signal is expressed as,

$$\phi(t) = \frac{B}{2T}t^2 + \left(f_c - \frac{B}{2}\right)t \quad (2)$$

where B is the sweeping bandwidth, T is the time duration, and f_c is the center frequency of the chirp signal.

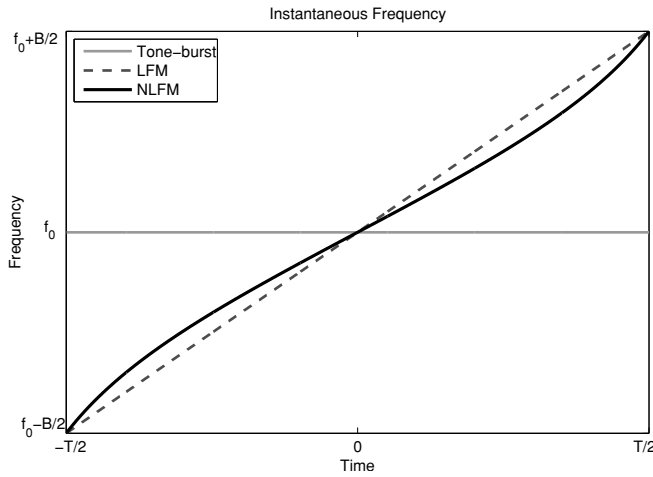


Fig. 1. The figure shows the instantaneous frequencies of a LFM, NLFM, and tone-burst signals with a signal duration of T . The tone-burst signal has a constant frequency of f_0 . The LFM and NLFM signals are linearly and nonlinearly sweeping the frequency range of $f_0 - B/2$ and $f_0 + B/2$, respectively.

The instantaneous frequency of the LFM signal can be found by calculating the time derivative of the phase modulation function, $f_i(t) = \phi'(t)$. The second derivative of the phase modulation function gives the chirp-rate of the signal, $a = \phi''(t) = B/T$.

B. Nonlinear Frequency Modulated (NLFM) Signals

NLFM signals can be designed to have a predetermined spectral response without any temporal limitations [37]. This allows the NLFM signal to provide more flexibility in signal design and SNR improvement than the LFM signal, where the spectrum is determined by the applied window function in the time domain. The power spectrum of the NLFM signal can be designed by choosing a suitable window function which provides reduced sidelobes level after pulse compression. Although NLFM signals have certain advantages over LFM signals, the design process is more complicated. In this study, an analytical technique is used to design the NLFM signal. The NLFM signal can be expressed as

$$\begin{aligned} x_n(t) &= p(t) e^{j2\pi\phi_n(t)}, \quad 0 \leq t \leq T \\ x_n(t) &= 0, \quad \text{else} \end{aligned} \quad (3)$$

where $p(t)$ and $\phi_n(t)$ are the amplitude modulation and phase modulation functions.

In the case of a LFM signal, the shape of the power spectrum is modified by altering the amplitude modulation function. For the NLFM, the chirp-rate function is used to shape the power spectrum. However in this work, the NLFM signals are designed using a ‘‘hybrid design approach’’ by modifying both the chirp-rate and amplitude modulation functions. The hybrid designed NLFM signal is less sensitive to Doppler shift caused by the moving tissue or blood than LFM signal with an expense of reduced SNR [38].

According to the principle of stationary phase, the power

spectrum of the chirp signal is approximately equal to [39],

$$|X(f)|^2 \approx \frac{p^2(t)}{|a_n(t)|}, \quad (4)$$

where $|X(f)|^2$ is the power spectrum and $a_n(t)$ is the chirp-rate function of the signal. A Hann window is selected as a desired shape of the NLFM power spectrum, which is expressed as [40],

$$|X(f)|^2 = \frac{1}{2} \left[1 - \cos \left(2\pi \frac{t}{T} \right) \right], \quad 0 \leq t \leq T. \quad (5)$$

The nonlinear instantaneous frequency function, $f_i(t)$, containing the linear and tangential frequency modulation functions is expressed as [39],

$$f_i(t) = \phi'_n(t) = f_c + \frac{B}{2} \left[\frac{\alpha \tan(2\gamma t/T)}{\tan(\gamma)} + \frac{2(1-\alpha)t}{T} \right], \quad (6)$$

where parameters α and γ are adjusted to control the nonlinear frequency modulation curve. α is the ratio of nonlinear modulation and defined between $[0, 1]$. γ controls the tangential curve at the beginning and end of the signal and defined between $[0, \pi/2]$.

The chirp-rate function, $a_n(t)$, of the NLFM signal can be computed by either calculating the second derivative of the nonlinear phase modulation function, or calculating the derivative of the nonlinear instantaneous frequency function, $f_i(t)$, in Eq. (6) as

$$a_n(t) = \phi''_n(t) = \frac{B}{T} \left[\frac{\alpha\gamma (1 + \tan^2(2\gamma t/T))}{\tan(\gamma)} + (1-\alpha) \right]. \quad (7)$$

The amplitude modulation function, $p(t)$, of the NLFM signal can be obtained by rearranging the Eq. (4),

$$p(t) = \sqrt{|X(f)|^2 |a_n(t)|}. \quad (8)$$

The phase modulation function, $\phi_n(t)$, of the NLFM signal can be obtained by computing the integral of the nonlinear instantaneous frequency function, $f_i(t)$, using Eq. (6);

$$\phi_n(t) = f_c t + \frac{B}{2} \left[\frac{-T\alpha \ln |\cos(2\gamma t/T)|}{2\gamma \tan(\gamma)} + \frac{(1-\alpha)t^2}{T} \right]. \quad (9)$$

Finally, substituting the values of amplitude modulation function $p(t)$, and the phase modulation function $\phi_n(t)$ into Eq. (3) will produce the NLFM signal.

The instantaneous frequencies of the excitation signals are shown in Figure 1 to illustrate the main difference between tone-burst, LFM and NLFM waveforms. The shape of instantaneous frequency function of the NLFM waveform was shaped by the signal parameters $\alpha = 0.52$ and $\gamma = 1.1$, where the reason for choosing these values will be detailed in the next section.

C. Effect of Tapering by a Window Function

In ultrasound imaging with chirp excitation the signal’s envelope is set by a window function, which can control the spectral leakage of the transmit signal. The leakage of the transmitted energy to lower frequencies will decrease the

TABLE I
COMPARISON OF VARIOUS WINDOWS

WINDOW	Coherent Gain (normalized)	Highest* Sidelobe Level (dB)	Sidelobe* Roll-off (dB/octave)	-6.0 dB Mainlobe Width (1/B)	
Rectangular	1.00	-13	-6	1.21	
NLFM [†]	0.64	-44	-12	2.44	
Hann	0.50	-32	-18	2.58	
Blackman	0.42	-58	-18	3.10	
Hamming	0.54	-43	-6	2.41	
Gaussian	$a=2.5$	0.51	-42	-6	2.64
	$a=3.0$	0.43	-55	-6	3.15
	$a=3.5$	0.37	-69	-6	3.66
Dolph-Chebyshev	$a=2.5$	0.53	-50	0	2.35
	$a=3.0$	0.48	-60	0	2.70
	$a=3.5$	0.45	-70	0	2.94
Kaiser-Bessel	$a=4.0$	0.42	-80	0	3.15
	$a=2.0$	0.49	-46	-6	2.64
	$a=2.5$	0.44	-57	-6	2.95
Bessel	$a=3.0$	0.40	-69	-6	3.25
	$a=3.5$	0.37	-82	-6	3.52

* The highest sidelobe level and the sidelobe roll-off determine the spectral leakage.

[†] The custom window designed with Eq. (8) for the NLFM excitation with $\gamma = 1.1$ and $\alpha = 0.52$.

image CTR on subharmonic imaging and must be minimized. On the receiver side, this window function also determines the mainlobe width and the sidelobe levels after pulse compression. Image dynamic range and image resolution can be improved by reducing the sidelobe levels and the mainlobe width of the pulse compressed signal, respectively. In the selection process of the tapering window, there is always a trade-off between sidelobe levels, mainlobe width and spectral leakage.

In this work, the main purpose of using windows was to reduce the spectral leakage, while maintaining a high coherent gain. Some of the widely used window functions, such as rectangular, Hamming, Hann, Blackman, Gaussian, Dolph-Chebyshev, and Kaiser-Bessel were compared in terms of spectral leakage, resolution and windowing gain. The numerical comparison of these figures of merits are listed in Table I, where the values for coherent gain, highest sidelobe level and sidelobe roll-off are taken from [40].

Coherent Gain: The coherent gain is the sum of window coefficients that can be referred to as the DC gain of the window. For a rectangular window this gain is equal to the number of samples, N . For other windows, the gain is lower due to the window values being reduced to zero near the boundaries. From a perspective of subharmonic imaging, higher values of coherent gain will result in higher subharmonic generation since the total energy of the windowed waveform is proportional to the coherent gain. The coherent gain values normalized by N are listed in the Table I.

Spectral Leakage: The spectral leakage of a window function is directly related to its *sidelobe roll-off* and *highest sidelobe level* in frequency domain, where these values for different window functions are given in Table I. Minimizing both

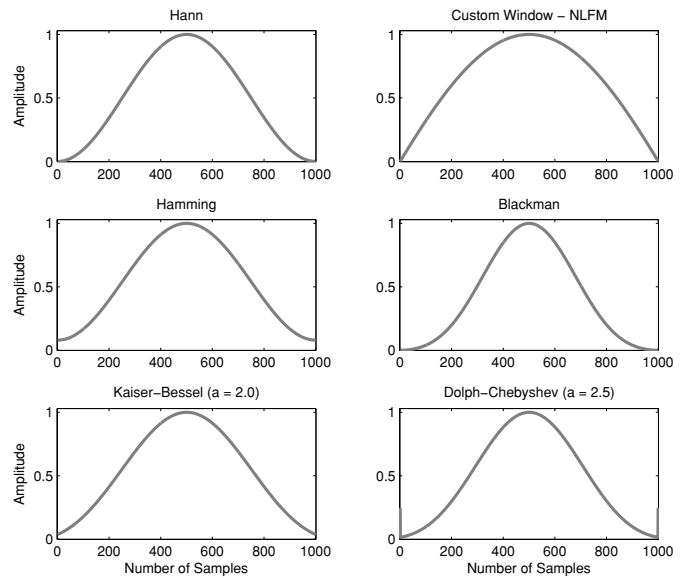


Fig. 2. Figure shows the shape of window functions for some of the common windows. (Top-Left) the Hann window, (Top-Right) the custom window designed with Eq. (8) for the NLFM excitation with $\gamma = 1.1$ and $\alpha = 0.52$, (Middle-Left) the Hamming window, (Middle-Right) the Blackman window, (Bottom-Left) the Kaiser-Bessel window ($a = 2.0$), and (Bottom-Right) the Dolph-Chebyshev window ($a = 2.5$).

of these metrics, while maintaining a high window coherent gain is crucial for all types of harmonic imaging. Therefore, the chirp waveforms with different window function were analyzed according to windows' capability of reducing the spectral leakage for subharmonic imaging with the parameters used in this study.

The main cause of spectral leakage is discontinuities in the signal. Discontinuities cause the signal's energy to leak from the center frequency, where the actual signal's energy exists, to adjacent frequencies. A window function can eliminate the discontinuities and reduce the spectral leakage by decreasing the signal's amplitude to zero at the beginning and end of the waveform [40].

In order to illustrate the effect of window shape on spectral leakage, some of the aforementioned window functions are plotted in Figure 2. The Hann window and the Blackman window are better candidates to prevent spectral leakage thanks to the reduction of the window coefficients to zero at the beginning and end of the function. These windows also have the highest sidelobe roll-off values of -18 dB when compared with the other window functions in Table I. The windows with shoulders such as Hamming, Kaiser-Bessel, and Dolph-Chebyshev usually have a higher spectral leakage, because they cannot completely cancel these discontinuities.

Figure 3 shows the signal spectra for a chirp waveform centered at f_0 , where the spectral leakage to the subharmonic frequency can be observed at $f_0/2$. The signal spectra for all waveforms were calculated by using Welch's method of power spectral density estimation to control the bias and variance of the estimated spectrum [41]. The window functions without shoulders contain less energy at $f_0/2$, therefore the chirp waveforms with Hann and the Blackman windows result in

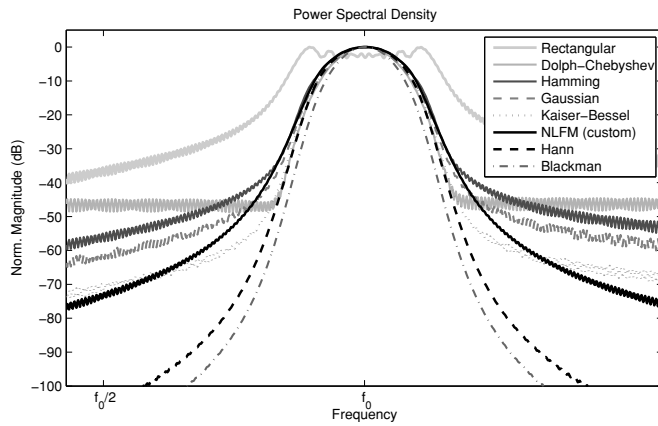


Fig. 3. Figure shows the spectra of chirp waveforms with rectangular, Dolph-Chebyshev ($a = 2.5$), Hamming, Gaussian ($a = 2.5$), Kaiser-Bessel ($a = 2.0$), Blackman, and Hann windows and a custom window designed for NLFM excitation with $\gamma = 1.1$ and $\alpha = 0.52$. The duration and bandwidth of signals shown in this figure are the same with the parameters used in subharmonic imaging experiments.

less spectral leakage to the subharmonic frequency.

−6 dB Mainlobe Width: In imaging applications, to distinguish between closely spaced objects short duration pulses are preferred. For the case of chirp coded excitation and pulse compression on the receive, the signal's autocorrelation function is the major factor that determines the resolution. For this reason, the −6 dB mainlobe width of the autocorrelation function was chosen as a comparison metric. To find the −6 dB width, windowed chirp signals were pulse compressed with a matched filter designed by using the same window function and the full width at half maximum point was measured. The calculated −6 dB mainlobe width for different window functions are listed in Table I, where units are normalized according to signal's sweeping bandwidth (B).

The window functions with narrower widths results in better resolution, but in higher sidelobes such as a rectangular window. The rectangular window achieves the best resolution with a −6 dB width of $1.21/B$, but it has the worst sidelobe performance with a highest sidelobe level of −13 dB. As the main lobe width narrows, the more energy is transferred to the sidelobes. On the other hand, the Hann window can only achieve a −6 dB width of $2.58/B$, but higher spectral leakage suppression with a highest sidelobe level of −32 dB and a sidelobe roll-off of −18 dB. For this reason, the Hann window performs better than most of the window functions in terms of energy leakage at the subharmonic frequency range as given in Figure 3 and thus it is one of the most commonly preferred window functions.

D. Designing a Custom Windowed NLFM Signal

In this study, a composite image structure was used and subharmonic and fundamental B-mode images were overlaid. Therefore, the selection of window function was based on spectral leakage and coherent gain instead of focusing on improving the image resolution. For this reason, the Hann window with a moderate −6 dB mainlobe width of $2.58/B$ was chosen as the golden standard.

In order to choose a suitable window function for subharmonic imaging, the window functions were first compared according to −6 dB width of their autocorrelation function. The window functions with wider mainlobe widths than the Hann window was eliminated from the list. After that, the Hamming, Kaiser-Bessel ($a = 2.0$), Gaussian ($a = 2.5$) and Dolph-Chebyshev ($a = 2.5$) windows were compared according to their spectral leakage and coherent gain. However, none of these window functions give more than 6% improvement in terms of coherent gain, which will increase the total energy of the excitation signal and hence the subharmonic response from microbubbles. Therefore, a NLFM waveform with a custom window was designed by using Eq. (8). The ratio of nonlinear modulation was chosen to be 0.5, which is the main factor that determines the main lobe width. By selecting $\alpha = 0.5$ a similar resolution with a Hann windowed LFM chirp can be achieved. Later the γ was found to be 1.1 in order to maximize the coherent gain while keeping the spectral leakage level below the noise floor of the imaging system used in this study, which was -63 ± 3 dB. After designing the NLFM signal, the α was changed as 0.52 to compensate for the truncation errors.

The final NLFM signal, which was designed with $\alpha = 0.52$ and $\gamma = 1.1$, had a −6 dB bandwidth of $2.44/B$, a coherent gain of 0.64, and a spectral leakage at $f_0/2$ of −72 dB, which is the average noise floor (−63 dB) plus three standard deviations (−3 dB). The choice of this window function was result of a compromise between coherent gain, resolution and spectral leakage as explained above. Note that the available window functions in the literature are not limited to those listed in Table I, but the same trade-off on coherent gain, resolution and spectral leakage applies to all window functions.

III. MATERIALS AND METHODS

In this study, two experiments were performed by using a custom windowed NLFM excitation. In the first experiment, the subharmonic response of UCAs was measured based on the scattered pressure from a microbubble population. For the second experiment an ultrasound flow phantom was built, and subharmonic and fundamental B-mode images were captured with a medical probe. For both experiments the results achieved by the NLFM chirp with a customized window was compared to a Hann windowed LFM chirp, which was considered to be the golden standard due to its low spectral leakage.

A. Microbubble Manufacture

The lipids were prepared by mixing 18.5 μl of 1,2-Dipalmitoyl-*sn*-glycero-3-phosphocholine (DPPC), 6.6 μl of 1,2-Distearoyl-*sn*-glycero-3-phosphoethanolamine-N-[maleimide(polyethylene glycol)-2000] (DSPE-PEG2000), and 16.3 μl of 1,2-Dipalmitoyl-*sn*-glycero-3-phosphate (DPPA) from Avanti Polar Lipids (Alabaster, AL) dissolved in chloroform and drying them in a glass vial within a vacuum desiccator. Microbubbles were prepared by re-suspending the lipids in Dulbecco's Phosphate-Buffered Saline (DPBS) containing 1% glycerin by volume in an ultrasound bath (U50, Ultrawave Ltd, Cardiff, UK). This solution was mixed

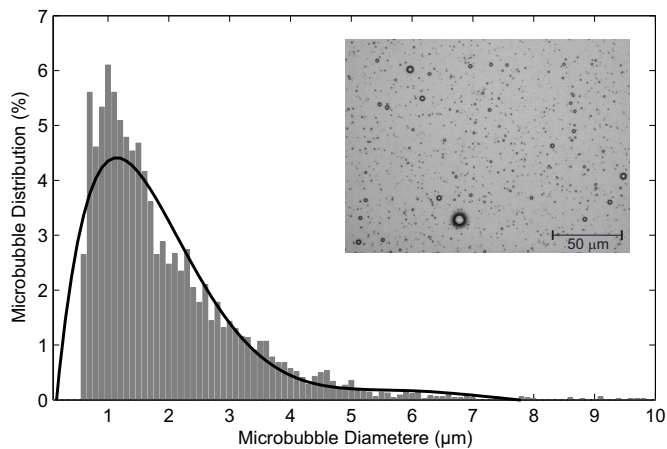


Fig. 4. The histogram of microbubble size distribution measured with a microscope. The black line is a polynomial fit over the histogram. A typical micrograph of manufactured microbubbles is shown on top-right corner of the graph.

in a 1 ml vial and saturated with C_3F_8 , which forms the gas core. The vial was shaken for 45 seconds by a CapMix mechanical shaker (3M ESPE, St. Paul, MN).

After producing the microbubbles, their size distribution and concentration were optically measured by Nikon Eclipse Ti-U inverted microscope (Nikon Corp, Tokyo, Japan) [42] as shown in Figure 4. The average diameter and the concentration of the manufactured microbubbles were $1.9 \pm 1 \mu\text{m}$ and 1×10^{10} MB/ml, respectively. The microbubbles were diluted with deionized water by 1:5000 to achieve similar concentrations to those observed in the human body. The scattering response of the diluted microbubble solution was measured for the frequency range of 3 – 8 MHz at a peak-negative pressure (PNP) of 100 kPa. The resonance frequency of the microbubble population was measured as 3.8 MHz.

B. Measuring the Subharmonic Emission from Microbubbles

The ultrasound scattering from UCAs was measured as a function of applied acoustic pressure and signal bandwidth. Different waveforms were tested to assess the effect of waveform and window function on subharmonic emissions from microbubbles. The pressure range of 100 – 600 kPa PNP was used for the measurements performed by a Hann windowed sinusoidal tone-burst, Hann windowed LFM chirp, and custom windowed NLFM chirp. All excitation signals were designed with a center frequency of 7.6 MHz, which was twice the resonance frequency of the microbubble population used in this study, and a signal duration of 20 μs . To show the effect of the excitation bandwidth on subharmonic generation from UCAs, the LFM and the NLFM waveforms were designed with fractional bandwidths of 10%, 20% and 40% and compared with a tone-burst excitation.

All acoustic measurements were conducted in an acrylic tank containing deionized and degassed water at 20°C as shown in Figure 5. A cylindrical chamber containing the microbubble suspension was immersed in a water tank. The chamber had an internal diameter of 25 mm and had windows covered by acoustically transparent saran wrap. Two of these

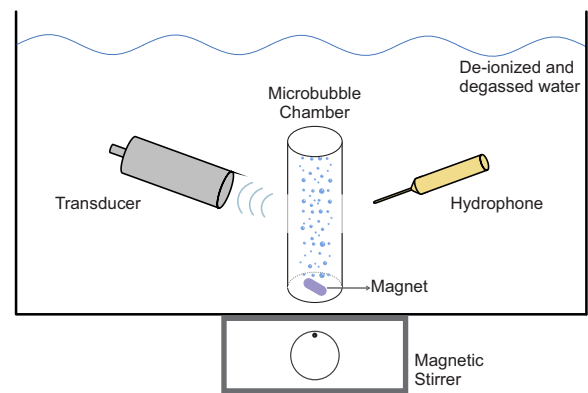


Fig. 5. The illustration of the experimental setup used to measure subharmonic scattering from UCAs. The transducer was positioned perpendicular to the hydrophone, where both equipment were facing an acoustically transparent window.

windows were facing the transmitting transducer to let the acoustic field in and out, and another facing the receiving hydrophone. The weakly focused transducer was positioned with a distance of 10 mm from the chamber in the acrylic tank, in order to have the microbubble chamber in the focal region of the transducer. The hydrophone was placed perpendicular to the transducer and was aligned to the focal region. The suspension was continuously mixed using a magnetic stirrer to ensure uniform microbubble distribution during the measurements. A fresh microbubble suspension was used for each set of measurements.

All excitation signals were designed in Matlab (Mathworks Inc., Natick, MA) and then loaded into a 33250A Arbitrary Waveform Generator (Agilent Technologies Inc., Santa Clara, CA). The generated signals were amplified with an A150 RF Power Amplifier (Electronics & Innovation Ltd., Rochester, NY) and then used to drive a single element V310 immersion transducer (Olympus-NDT Inc., Waltham, MA), which has a center frequency of 5 MHz and a -6 dB fractional bandwidth of 80%. The pressure calibration of the transducer was performed using a Polyvinylidene Difluoride (PVDF) 1 mm needle hydrophone (Precision Acoustics Ltd., Dorchester, UK). Transmit waveforms were pre-distorted according to the frequency response of the transducer [43], [44]. Before each microbubble scattering measurement the noise floor was determined for each pressure level, by performing a control measurement without microbubbles in the chamber.

For each excitation signal and acoustic pressure, 150 measurements were taken with a pulse repetition frequency of 100 Hz. The scattered pressure from contrast agents were received using the 1 mm needle hydrophone. The received signals were amplified by 40 dB using a 5072-PR pre-amplifier (Panametrics-NDT, Inc., Waltham, MA) and digitized at a sampling frequency of 1 GHz using a 8-bit LeCroy 64xi digital oscilloscope (LeCroy Corporation, Chestnut Ridge, NY). After downloading the data to a PC, all received signals were converted into pressure values in Matlab using the frequency response of the hydrophone with the calibration data supplied by the manufacturer. The received signals spectra were averaged in the frequency domain over the 150 measurements to

reduce the variance of the experimental results due to multiple scattering effects from the microbubble cluster, low signal amplitude, and large fluctuations as a result of microbubble movements [45].

C. Ultrasound Phantom

A wall-less flow phantom was manufactured by using tissue mimicking material (TMM) to capture B-mode images of UCAs in flow. The TMM was prepared by mixing 3% (36 g.) high strength Agar powder (Acros Organics, Geel, Belgium), 10 g. Germall plus (ISP Chemicals LLC, Chatham, NJ), 25 g. soda-lime glass microspheres with a diameter $\leq 25 \mu\text{m}$ (MO-SCI Corp., Rolla, MO), and 87% de-ionized water by volume. The solution was heated in a Compact 40 benchtop autoclave (Priorclave Ltd., London, UK) at 96°C for 30 minutes. When temperature was below 70°C , 8% glycerin was added to the solution and poured into a special phantom holder with a 5 mm thick stainless steel rod. To remove the air from the mixture, it was put in a desiccator under vacuum for 2 hours. After the TMM was set, the steel rod was removed to create the wall-less vessel. The attenuation and average sound velocity in the TMM were measured as $0.56 \text{ dB/cm}\cdot\text{MHz}$ and 1524 m/s , respectively.

D. Imaging Setup

An Ultrasound Array Research Platform (UARP) was used to capture fundamental and subharmonic B-mode images of the TMM phantom. The UARP is a custom 96-channel ultrasound imaging system developed by the Ultrasound Group at the University of Leeds [46], [47]. It is a highly flexible system based on an Altera Stratix III FPGA (Altera Corporation, San Jose, CA, USA), and capable of simultaneous excitation on 96 channels with arbitrary waveforms and transfer of the received raw RF data from individual channels to a computer.

A L3-8/40EP medical probe (Prosonic Co., Korea) was connected to the UARP to perform a linear scan of the flow phantom. The -6 dB bandwidth of the medical probe was approximately $3 - 8 \text{ MHz}$. For this reason, the excitation waveforms were transmitted at $6 - 8 \text{ MHz}$ so that the subharmonic can be received by the same probe at the frequency range of $3 - 4 \text{ MHz}$. To demonstrate the effect of excitation waveform on subharmonic imaging three waveforms were designed and tested; a rectangular windowed LFM chirp, a Hann windowed LFM chirp, and a custom windowed NLFM chirp with parameters of $\gamma = 1.1$ and $\alpha = 0.52$. Therefore, the UARP was programmed to generate three chirp waveforms with a center frequency of 7 MHz , duration of $20 \mu\text{s}$, and bandwidth of 2 MHz for subharmonic imaging. To compensate for the transducer response and to keep the original window shapes, transmit waveforms were pre-distorted according to the frequency response of the medical probe [43], [44].

The experimental setup for fundamental and subharmonic imaging is illustrated in Figure 6. To capture individual B-mode frames, the medical probe was electronically focused to the wall-less vessel inside the flow phantom at a depth of 40 mm . The UCAs were injected using a 20 ml syringe containing a $10 \mu\text{l}$ suspension of microbubbles ($\sim 5 \times 10^6 \text{ MB/ml}$)

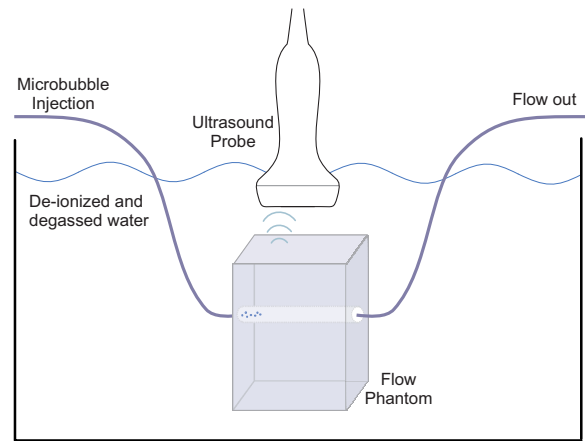


Fig. 6. The illustration of the experimental setup used to capture fundamental and subharmonic images shown in Figures 9, 10 and 11.

in one minute. A linear scan was performed by the UARP at 1 MPa PNP in the focal region, where microbubbles only experienced 630 kPa PNP due to the attenuation in TMM.

Two different sets of measurements were performed for each excitation signal by repeating the same experimental procedure. On each measurement 25 B-mode frames were captured to compare the average contrast improvement according to the choice of window function. The captured data was stored in a computer and processed off-line using Matlab. All received signals were corrected using an inverse filter according to the frequency response of the medical probe.

The pulse compression was performed on each beamformed scan line by a matched filter to form the fundamental B-mode images and by a subharmonic matched filter to form the subharmonic images. The matched filter had the same signal parameters with the excitation waveform and the subharmonic matched filter was designed with a center frequency of 3.5 MHz and a bandwidth of 1 MHz . The pulse compression of the subharmonic component was possible with a subharmonic matched filter, since the harmonic component of the chirp is also chirp because they maintain their coded phase relation in the harmonic domain [36].

IV. EXPERIMENTAL RESULTS

A. Subharmonic Generation with LFM and NLFM

Subharmonic behavior of UCAs was investigated as a function of acoustic pressure for sinusoidal tone-burst, LFM and NLFM signals. Figure 7(top) shows a typical scattered pressure wave from the diluted microbubble solution for NLFM chirp excitation with 40% fractional bandwidth at 600 kPa PNP. The spectra of these measurements were used to calculate the total subharmonic power above the noise threshold, where Figure 7(bottom) shows the signal spectra for various excitation pressures. The results were analyzed after averaging 150 measurements in the spectral domain, where the average noise floor of 150 control measurements was $4.35 \pm 2.34 \text{ Pa}$. The quantitative results shown in Figure 8 represent the SNR in the subharmonic band that can be used for subharmonic imaging ($p < 0.001$).

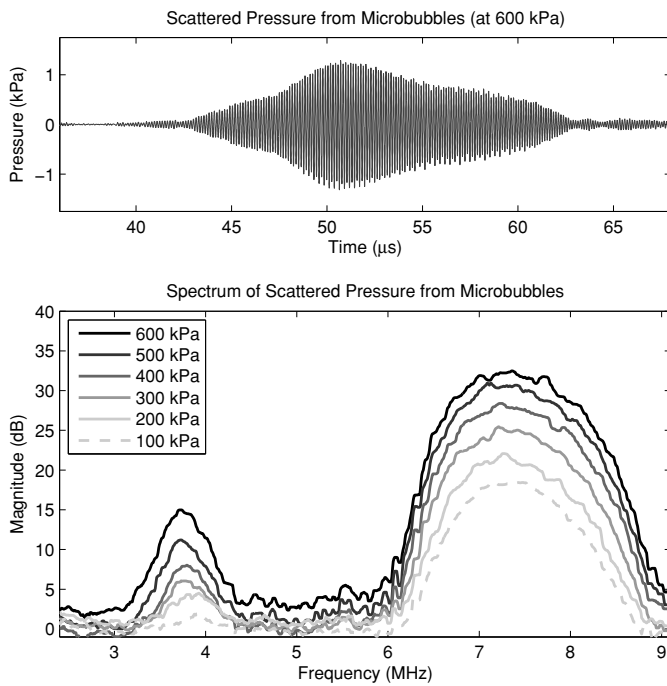


Fig. 7. (Top) A typical scattered signal from microbubbles for NLFM chirp excitation with 40% fractional bandwidth at 600 kPa PNP. (Bottom) Spectra of the scattered signal from microbubbles for NLFM excitation with 40% fractional bandwidth at a pressure range of 100 – 600 kPa PNP.

For low pressure levels (100 – 300 kPa PNP), the noise levels were higher than the measurements performed at higher pressure levels. Therefore the total signal power above the noise threshold in the subharmonic frequency band is larger for the narrowband signals. Since narrowband excitation signals have most of their energy confined into a narrower band, they can achieve higher peak levels above the noise floor even at low pressure. Therefore, at 100 kPa PNP the SNR for wideband LFM and NLFM chirp excitations were only 3.9 dB and 2.6 dB more than the tone-burst excitation.

For the experiments performed at high pressure levels (400 – 600 kPa PNP), the measurement error was lower as given by the standard deviation values in Figure 8. Therefore, the total subharmonic power was not affected by the noise level as much as low pressure measurements. Since wideband signals generate more subharmonic from UCA, the total scattered power is usually higher for the wideband signals. At high pressure levels, an average SNR improvement of 5.7 ± 1.6 dB was observed for wideband (40% fractional bandwidth) over narrowband (10% fractional bandwidth) chirp excitation at the subharmonic frequency band. At 600 kPa PNP, the SNR for wideband LFM and NLFM chirp excitations were approximately 12 dB and 15.4 dB more than the tone-burst excitation.

The results of the scattering measurements from UCAs indicate that the subharmonic response from microbubbles is strongly dependent on the excitation signal and applied acoustic pressure as previously reported in the literature [19], [20]. Increasing the excitation bandwidth of a fixed duration signal was spread the signal's energy to a wider spectral range and increased the likelihood of subharmonic generation from

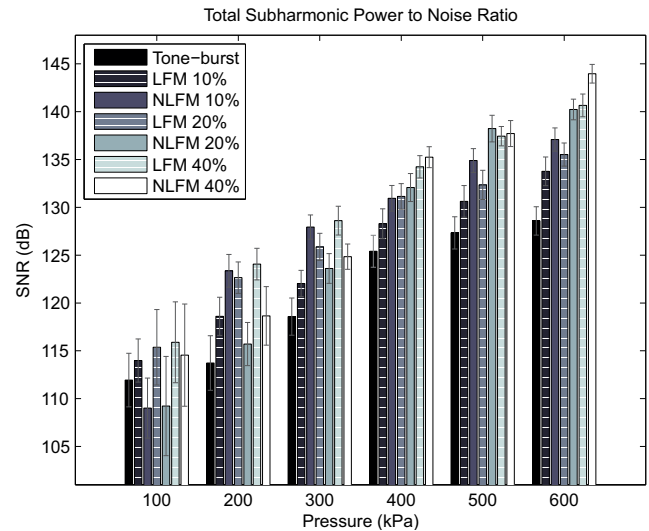


Fig. 8. Signal to noise ratio in the subharmonic band scattered from UCAs for tone-burst, LFM and NLFM excitations for pressure range of 100 – 600 kPa PNP. Gray lines show the standard deviation for each set of measurement.

a polydisperse population of microbubbles [48]. Increasing the signal's total energy by using a different amplitude modulation also improves the subharmonic response from UCAs. For this reason, the subharmonic energy for NLFM excitations was always higher than the LFM excitations for acoustic pressures of 400 kPa PNP and above for all bandwidths, which shows that the NLFM excitation is more suitable for subharmonic imaging.

B. Subharmonic Imaging

Figure 9, Figure 10 and Figure 11 each show four frames of composite images of the flow phantom captured with a rectangular windowed LFM chirp excitation, a Hann windowed LFM chirp excitation and a custom windowed NLFM chirp excitation, respectively. On these composite images, the subharmonic image is overlaid on a gray scale B-mode fundamental image for visualization of the phantom geometry. Subharmonic image has a dynamic range of 10 dB and represented with yellow-to-red colors. The grayscale fundamental image has a dynamic range of 40 dB. Frame 1 in these figures was captured as a control measurement without microbubbles. Frames 2, 3 and 4 were captured with microbubbles in flow during the beginning, middle and end of the UCA injection.

The first composite image was formed by rectangular windowed LFM chirp excitation as shown in Figure 9. Due to the high spectral leakage characteristic of the rectangular window, the fundamental energy existing in the subharmonic band results in strong echoes from the ultrasound phantom at subharmonic frequencies. These echoes appear as image artifacts, which can be observed in the frame 1 of Figure 9. In the later frames when microbubbles were injected into the ultrasound phantom, it is not possible to differentiate between microbubbles and image artifacts. Therefore, the rectangular windowed LFM chirp excitation is not suitable for subharmonic imaging.

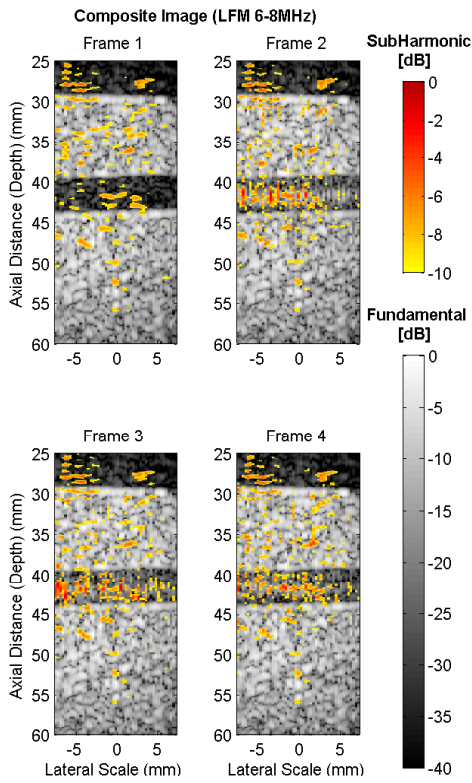


Fig. 9. Composite image of the flow phantom captured by using a rectangular windowed LFM excitation (Frame 1) without microbubbles and (Frames 2, 3, and 4) with microbubbles in flow.

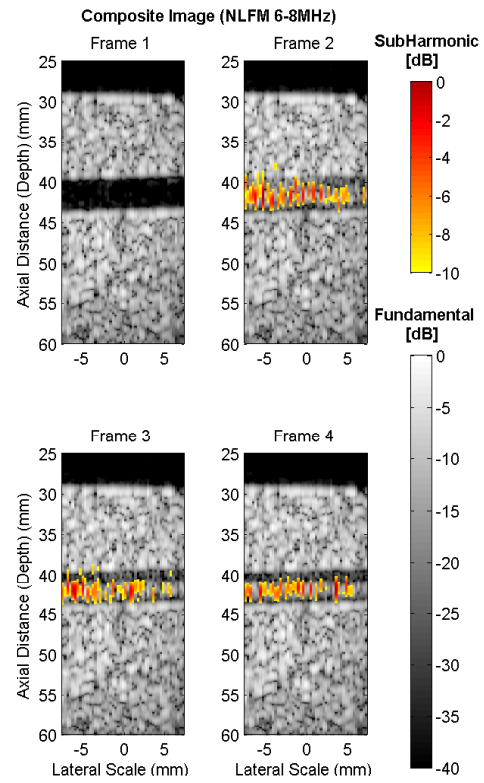


Fig. 11. Composite image of the flow phantom captured by using a custom windowed NLFM excitation (Frame 1) without microbubbles and (Frames 2, 3, and 4) with microbubbles in flow.

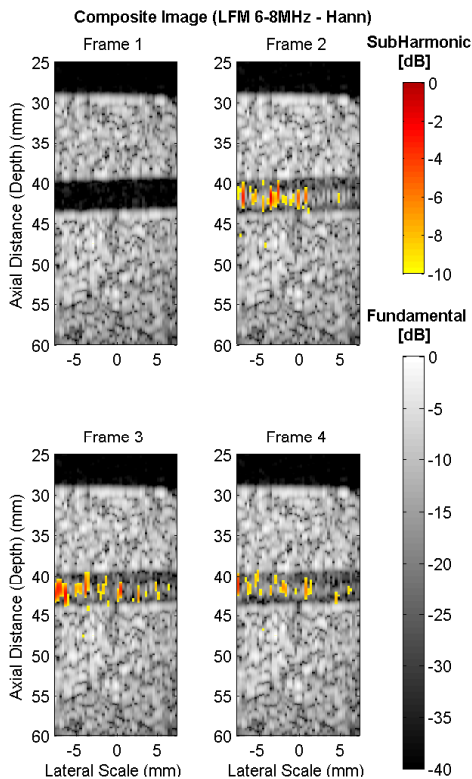


Fig. 10. Composite image of the flow phantom captured by using a Hann windowed LFM excitation (Frame 1) without microbubbles and (Frames 2, 3, and 4) with microbubbles in flow.

The Hann windowed LFM chirp excitation and the custom windowed NLFM chirp excitation can achieve a low spectral leakage in the subharmonic band. As a result of reduced spectral leakage, the reflections from within the TMM were suppressed in subharmonic images when compared to grayscale fundamental images. Therefore, no image artifacts are observed in frame 1 of Figure 10 and Figure 11. In the later frames when microbubbles were injected into the ultrasound phantom, it was observed that both excitation techniques can successfully detect the subharmonic emission from microbubbles.

To compare the results from both subharmonic images generated by a Hann windowed LFM chirp excitation and a custom windowed NLFM chirp excitation, RF data for 2 B-mode scans consisting of 25 frames each were processed. Each B-mode image was formed by 49 A-scan lines by linear scan of the flow phantom. The region covering the wall-less vessel between the axial depth of 40 – 44 mm were used to calculate the contrast-to-noise ratio (CNR) values from each image, effectively corresponding to $2 \times 25 \times 49$ scattering measurements. The CNR in the region of interest was found by calculating the ratio of average intensity value with microbubbles to average noise value, as defined by Hill *et. al.* [49]. The NLFM excitation showed an average CNR improvement of 4.35 ± 0.42 dB over Hann windowed LFM excitation for subharmonic imaging and the peak subharmonic CNR improvement was 5.46 dB.

V. DISCUSSION

Chirp coded excitation technique has been used in medical imaging to increase the SNR and penetration depth by utilizing wideband and long duration waveforms. For contrast-enhanced ultrasound imaging, the chirp excitation also enhances the ultrasound scattering from microbubble populations and can achieve a better CTR. Even though phospholipid coated commercial UCAs and in-house produced microbubbles have different behavior, subharmonic emission efficiency, and disruption threshold [25]; their response to wideband excitation will be stronger since UCAs have a polydisperse size distribution. More microbubbles can be excited close to their resonance frequency, which also increases the nonlinear behavior of microbubbles. To maximize the subharmonic response, however, a wideband excitation centered at twice the microbubble resonance frequency is necessary.

In order to verify this hypothesis, the subharmonic emissions from microbubbles were measured by using a single element transducer and a needle hydrophone. The excitation center frequency was selected as 7.6 MHz, since it was double the resonance frequency of the microbubbles used in this study. Instead of comparing the *peak subharmonic power* or *subharmonic-to-fundamental ratio*, which are commonly used for characterizing microbubbles and for measuring their nonlinear behaviors [48], [50], [51], the total subharmonic power was calculated to evaluate the subharmonic behavior of UCAs to different excitation signals. The reason for using this method was due to the variation in bandwidths of the LFM and NLFM chirps used in this study.

After analyzing the results of microbubble scattering experiments, it was discovered that the NLFM chirp excitation with 40% fractional bandwidth generates the highest subharmonic response. For this reason, the wideband NLFM signal was selected as an excitation waveform for subharmonic imaging. However, the medical probe used in experiments had a -6 dB bandwidth of 3 – 8 MHz, but waveforms with 40% fractional bandwidth was at the frequency range of 6.08 – 9.12 MHz. To overcome the frequency limitation imposed by the medical probe, the imaging waveforms were designed for the frequency range of 6 – 8 MHz.

Besides using wideband excitation, longer duration signals also enhance nonlinear oscillations from UCAs by increasing the total excitation energy. The design process of the chirp waveforms was also aimed at maximizing the duration of the signals to improve the SNR and penetration depth. Therefore, the time duration of excitation signals was chosen to be 20 μ s, which was another limitation imposed by the imaging system.

Another advantage of using long duration excitation can be more stable subharmonic response from UCAs without microbubble disruption, since disruption is more related to the peak negative pressure than to pulse length [28]. Shekhar and Doyle presented that using a rectangular window instead of a Gaussian shaped window will result in stronger subharmonic generation and lower subharmonic emission threshold. However for imaging applications, using a rectangular window will increase the spectral leakage to subharmonic frequencies as explained in section II-C. Therefore, a reduction in the CTR

was observed in Figure 9 when compared to Figure 10 and Figure 11 due to the reflections from tissue at subharmonic frequency. Therefore, reducing the spectral leakage by applying a window function is crucial for imaging applications even for the pulsed excitation. Eisenbrey *et. al.* used a modified commercial scanner for subharmonic imaging by using a 4-cycle pulse at 2.5 MHz [12]. Due to lack of windowing they have observed imaging artifacts similar to Figure 9 and reported strong broadband reflections from surfaces of the tissue phantom. In order to reduce these artifacts, they have implemented a pulse inversion (PI) scheme and achieved further suppression of tissue echoes.

Waveforms with rectangular envelopes can be used together with PI technique to increase the subharmonic emission and suppress the tissue response. All transmitted energy is cancelled after PI including the spectral leakage to the harmonic bands. PI and similar multiple excitation methods can cancel the effect of the fundamental component by halving the image frame rate. In the absence of tissue motion, the PI can achieve complete cancellation of the fundamental component that allows the use of whole transducer bandwidth. This significantly improves the image resolution for pulsed excitation; however for chirp excitation a tapering window is always necessary to reduce the sidelobe levels after pulse compression. Therefore, PI can only remove the image artifacts, but cannot further improve the spatial resolution and sidelobe levels for coded excitation.

In this study, all transmit waveforms were pre-distorted according to the transfer function of the medical probe and all received signals were corrected by an inverse filter designed with the frequency response of the medical probe. Although using custom designed arbitrary waveforms improve the overall performance of the ultrasound imaging system, it also increases the complexity of the transmit circuitry. In this study, to reduce the complexity of the transmitter, pulse width modulation and harmonic cancellation techniques with switched-mode excitation was utilized [52].

VI. CONCLUSION

The spectral leakage of the excitation signal's energy into subharmonic frequency is one of the main factors causing image degradation in subharmonic imaging. Spectral leakage must be minimized to reduce the energy leakage from the fundamental frequency component to the other frequencies, which increases the scattering from tissue at the subharmonic frequency and reduces the CTR. Similar conclusions were achieved by Shen and Li for tissue harmonic imaging [53]; to optimize imaging performance and maintain a high image contrast, the harmonic leakage needs to be minimized by controlling the frequency content of the waveform. Alternatively, multi-pulse excitation techniques such as pulse inversion can be utilized to suppress the fundamental signal. The pulse inversion method can completely cancel the spectral leakage to harmonic frequencies, but it suffers from motion artifacts and frame rate reduction.

Spectral leakage can be caused by system nonlinearities, harmonic distortion of the transmitter, and excitation wave-

form. In this study, the spectral leakage based on the transmit waveform was investigated for subharmonic imaging. A custom window function was used to control the tapering of the transmit waveform and its harmonic content. Window functions with high coherent gain generate more subharmonic emissions from microbubbles, but usually perform poorly in terms of spectral leakage and therefore degrade the image quality for subharmonic imaging. For this reason, a NLFM chirp waveform was designed to compromise between coherent gain, resolution and spectral leakage, since the NLFM method is more flexible thanks to design parameters α and γ . The experimental results showed that the custom windowed NLFM excitation generated more subharmonic emissions than the LFM excitation and improved the subharmonic image contrast.

REFERENCES

- [1] N. de Jong, M. Emmer, A. van Wamel, and M. Versluis, "Ultrasound characterization of ultrasound contrast agents," *Medical and Biological Engineering and Computing*, vol. 47, no. 8, pp. 861–873, 2009.
- [2] B. A. Schrope and V. L. Newhouse, "Second harmonic ultrasonic blood perfusion measurement," *Ultrasound in Medicine & Biology*, vol. 19, no. 7, pp. 567–579, 1993.
- [3] D. H. Simpson, C. T. Chin, and P. N. Burns, "Pulse inversion doppler: A new method for detecting nonlinear echoes from microbubble contrast agents," *Ultrasonics, Ferroelectrics and Frequency Control, IEEE Transactions on*, vol. 46, no. 2, pp. 372–382, 1999.
- [4] P. N. Burns, J. E. Powers, D. H. Simpson, A. Brezina, A. Kolin, C. T. Chin, V. Uhlendorf, and T. Fritzsche, "Harmonic power mode doppler using microbubble contrast agents: An improved method for small vessel flow imaging," in *IEEE Ultrasonics Symposium*, 1994, pp. 1547–1550.
- [5] R. Arshadi, A. C. H. Yu, and R. S. C. Cobbold, "Coded excitation methods for ultrasound harmonic imaging," *Canadian Acoustics*, vol. 35, no. 2, pp. 35–46, 2007.
- [6] P. D. Krishna, P. M. Shankar, and V. L. Newhouse, "Subharmonic generation from ultrasonic contrast agents," *Physics in Medicine and Biology*, vol. 44, no. 3, pp. 681–694, 1999.
- [7] F. Tranquart, N. Grenier, V. Eder, and L. Pouchot, "Clinical use of ultrasound tissue harmonic imaging," *Ultrasound in Medicine & Biology*, vol. 25, no. 6, pp. 889–894, 1999.
- [8] F. A. Duck, "Nonlinear acoustics in diagnostic ultrasound," *Ultrasound in Medicine & Biology*, vol. 28, no. 1, pp. 1–18, 2002.
- [9] F. Forsberg, W. T. Shi, and B. B. Goldberg, "Subharmonic imaging of contrast agents," *Ultrasonics*, vol. 38, no. 1–8, pp. 93–98, 2000.
- [10] J. Chomas, P. Dayton, D. May, and K. Ferrara, "Nondestructive subharmonic imaging," *Ultrasonics, Ferroelectrics and Frequency Control, IEEE Transactions on*, vol. 49, no. 7, pp. 883–892, 2002.
- [11] P. M. Shankar, P. D. Krishna, and V. L. Newhouse, "Advantages of subharmonic over second harmonic backscatter for contrast-to-tissue echo enhancement," *Ultrasound in Medicine & Biology*, vol. 24, no. 3, pp. 395–399, 1998.
- [12] J. R. Eisenbrey, J. K. Dave, V. G. Halldorsdottir, D. A. Merton, P. Machado, J. B. Liu, C. Miller, J. M. Gonzalez, S. Park, S. Dianis, C. L. Chalek, K. E. Thomenius, D. B. Brown, V. Navarro, and F. Forsberg, "Simultaneous grayscale and subharmonic ultrasound imaging on a modified commercial scanner," *Ultrasonics*, vol. 51, no. 8, pp. 890–897, 2011.
- [13] F. Forsberg, J. Liu, W. T. Shi, J. Furuse, M. Shimizu, and B. B. Goldberg, "In vivo pressure estimation using subharmonic contrast microbubble signals: Proof of concept," *Ultrasonics, Ferroelectrics and Frequency Control, IEEE Transactions on*, vol. 52, no. 4, pp. 581–583, 2005.
- [14] W. T. Shi, F. Forsberg, J. S. Raichlen, L. Needleman, and B. B. Goldberg, "Pressure dependence of subharmonic signals from contrast microbubbles," *Ultrasound in Medicine & Biology*, vol. 25, no. 2, pp. 275–283, 1999.
- [15] J. Dave, V. Halldorsdottir, J. Eisenbrey, J. Liu, M. McDonald, K. Dickie, C. Leung, and F. Forsberg, "Noninvasive estimation of dynamic pressures in vitro and in vivo using the subharmonic response from microbubbles," *Ultrasonics, Ferroelectrics and Frequency Control, IEEE Transactions on*, vol. 58, no. 10, pp. 2056–2066, 2011.
- [16] D. E. Goertz, M. E. Frijlink, D. Tempel, R. Krams, N. de Jong, and A. F. van der Steen, "Subharmonic contrast intravascular ultrasound," in *IEEE Ultrasonics Symposium*, 2007, pp. 1065–1068.
- [17] A. Needles, O. Couture, and F. S. Foster, "A method for differentiating targeted microbubbles in real time using subharmonic micro-ultrasound and interframe filtering," *Ultrasound in Medicine & Biology*, vol. 35, no. 9, pp. 1564–1573, 2009.
- [18] J. R. Eisenbrey, A. Sridharan, P. Machado, H. Zhao, V. G. Halldorsdottir, J. K. Dave, J. Liu, S. Park, S. Dianis, K. Wallace, K. E. Thomenius, and F. Forsberg, "Three-dimensional subharmonic ultrasound imaging in vitro and in vivo," *Academic Radiology*, vol. 19, no. 6, pp. 732–739, 2012.
- [19] E. Biagi, L. Breschi, E. Vannacci, and L. Masotti, "Subharmonic emissions from microbubbles: effect of the driving pulse shape," *Ultrasonics, Ferroelectrics and Frequency Control, IEEE Transactions on*, vol. 53, no. 11, pp. 2174–2182, 2006.
- [20] D. Zhang, Y. Gong, X. Gong, Z. Liu, K. Tan, and H. Zheng, "Enhancement of subharmonic emission from encapsulated microbubbles by using a chirp excitation technique," *Physics in Medicine and Biology*, vol. 52, no. 18, pp. 5531–5544, 2007.
- [21] D. Zhang, X. Xi, Z. Zhang, X. Gong, G. Chen, and J. Wu, "A dual-frequency excitation technique for enhancing the sub-harmonic emission from encapsulated microbubbles," *Physics in Medicine and Biology*, vol. 54, no. 13, pp. 4257–4272, 2009.
- [22] H. J. Vos, D. E. Goertz, A. F. W. van der Steen, and N. de Jong, "Parametric array technique for microbubble excitation," *Ultrasonics, Ferroelectrics and Frequency Control, IEEE Transactions on*, vol. 58, no. 5, pp. 924–934, 2011.
- [23] C. Shen, C. Cheng, and C. Yeh, "Phase-dependent dual-frequency contrast imaging at sub-harmonic frequency," *Ultrasonics, Ferroelectrics and Frequency Control, IEEE Transactions on*, vol. 58, no. 2, pp. 379–388, 2011.
- [24] N. de Jong, M. Emmer, C. T. Chin, A. Bouakaz, F. Mastik, D. Lohse, and M. Versluis, "Compression-only behavior of phospholipid-coated contrast bubbles," *Ultrasound in Medicine & Biology*, vol. 33, no. 4, pp. 653–656, 2007.
- [25] B. L. Helfield, E. Chérin, F. S. Foster, and D. E. Goertz, "Investigating the subharmonic response of individual phospholipid encapsulated microbubbles at high frequencies: A comparative study of five agents," *Ultrasound in Medicine & Biology*, vol. 38, no. 5, pp. 846–863, 2012.
- [26] T. Faez, M. Emmer, K. Kooiman, M. Versluis, A. F. W. van der Steen, and N. de Jong, "20 years of ultrasound contrast agent modeling," *Ultrasonics, Ferroelectrics and Frequency Control, IEEE Transactions on*, vol. 60, no. 1, pp. 7–20, 2013.
- [27] A. Eller and H. G. Flynn, "Generation of subharmonics of order one-half by bubbles in a sound field," *The Journal of the Acoustical Society of America*, vol. 46, no. 3B, pp. 722–727, 1969.
- [28] H. Shekhar and M. M. Doyley, "Improving the sensitivity of high-frequency subharmonic imaging with coded excitation: A feasibility study," *Medical Physics*, vol. 39, no. 4, pp. 2049–2060, 2012.
- [29] V. Daeichin, T. Faez, G. Renaud, J. G. Bosch, A. F. W. van der Steen, and N. de Jong, "Effect of self-demodulation on the subharmonic response of contrast agent microbubbles," *Physics in Medicine and Biology*, vol. 57, no. 12, pp. 3675–3691, 2012.
- [30] FDA, "Information for manufacturers seeking marketing clearance of diagnostic ultrasound systems and transducers," FDA, Tech. Rep., 30-09-1997.
- [31] C. E. Cook and M. Bernfeld, *Radar signals: An introduction to theory and application*. New York: Academic Press, 1967.
- [32] R. Chiao and X. Hao, "Coded excitation for diagnostic ultrasound: a system developer's perspective," *Ultrasonics, Ferroelectrics and Frequency Control, IEEE Transactions on*, vol. 52, no. 2, pp. 160–170, 2005.
- [33] S. Harput, "Use of chirps in medical ultrasound imaging," Ph.D. Thesis, University of Leeds, UK, 2012.
- [34] C. Leavens, R. Williams, F. S. Foster, P. N. Burns, and M. D. Sherar, "Golay pulse encoding for microbubble contrast imaging in ultrasound," *Ultrasonics, Ferroelectrics and Frequency Control, IEEE Transactions on*, vol. 54, no. 10, pp. 2082–2090, 2007.
- [35] C. Shen and T. Shi, "Golay-encoded excitation for dual-frequency harmonic detection of ultrasonic contrast agents," *Ultrasonics, Ferroelectrics and Frequency Control, IEEE Transactions on*, vol. 58, no. 2, pp. 349–356, 2011.
- [36] T. Misaridis and J. A. Jensen, "Use of modulated excitation signals in medical ultrasound. part ii: Design and performance for medical imaging applications," *Ultrasonics, Ferroelectrics and Frequency Control, IEEE Transactions on*, vol. 52, no. 2, pp. 192–207, 2005.

- [37] M. Pollakowski and H. Ermert, "Chirp signal matching and signal power optimization in pulse-echo mode ultrasonic nondestructive testing," *Ultrasonics, Ferroelectrics and Frequency Control, IEEE Transactions on*, vol. 41, no. 5, pp. 655–659, 1994.
- [38] J. A. Johnston and A. C. Fairhead, "Waveform design and doppler sensitivity analysis for nonlinear fm chirp pulses," *Communications, Radar and Signal Processing, IEE Proceedings F*, vol. 133, no. 2, pp. 163–175, 1986.
- [39] T. Collins and P. Atkins, "Nonlinear frequency modulation chirps for active sonar," *Radar, Sonar and Navigation, IEE Proceedings*, vol. 146, no. 6, pp. 312–316, 1999.
- [40] F. J. Harris, "On the use of windows for harmonic analysis with the discrete Fourier transform," *Proceedings of the IEEE*, vol. 66, no. 1, pp. 51–83, 1978.
- [41] P. D. Welch, "The use of fast fourier transform for the estimation of power spectra: A method based on time averaging over short, modified periodograms," *Audio and Electroacoustics, IEEE Transactions on*, vol. 15, no. 2, pp. 70–73, 1967.
- [42] J. McLaughlan, N. Ingramy, P. R. Smith, S. Harput, P. L. Coletta, S. Evans, and S. Freear, "Increasing the sonoporation efficiency of targeted polydisperse microbubble populations using chirp excitation," *Ultrasonics, Ferroelectrics and Frequency Control, IEEE Transactions on*, In Press.
- [43] T. Misaridis and J. Jensen, "An effective coded excitation scheme based on a predistorted FM signal and an optimized digital filter," in *IEEE Ultrasonics Symposium*, 1999, pp. 1589–1593.
- [44] P. R. Smith, S. Harput, D. M. J. Cowell, J. McLaughlan, and S. Freear, "Pre-distorted amplitude modulated (PDAM) chirps for transducer compensation in harmonic imaging," in *IEEE Ultrasonics Symposium*, 2012, pp. 459–462.
- [45] J. Gorce, M. Arditì, and M. Schneider, "Influence of bubble size distribution on the echogenicity of ultrasound contrast agents: A study of sonovue," *Investigative Radiology*, vol. 35, no. 11, pp. 661–671, 2000.
- [46] D. M. J. Cowell and S. Freear, "Quinary excitation method for pulse compression ultrasound measurements," *Ultrasonics*, vol. 48, no. 2, pp. 98–108, 2008.
- [47] P. R. Smith, D. M. J. Cowell, B. Raiton, C. V. Ky, and S. Freear, "Ultrasound array transmitter architecture with high timing resolution using embedded phase-locked loops," *Ultrasonics, Ferroelectrics and Frequency Control, IEEE Transactions on*, vol. 59, no. 1, pp. 40–49, 2012.
- [48] S. Harput, M. Arif, and S. Freear, "Experimental investigation of the subharmonic emission from microbubbles using linear and nonlinear frequency modulated signals," in *IEEE Ultrasonics Symposium*, 2010, pp. 1724–1727.
- [49] C. R. Hill, J. C. Bamber, and D. O. Cosgrove, "Performance criteria for quantitative ultrasonology and image parameterisation," *Clin. Phys. Physiol. Meas.*, vol. 11, no. A, pp. 57–73, 1990.
- [50] P. J. A. Frinking, E. Gaud, J. Brochot, and M. Arditì, "Subharmonic scattering of phospholipid-shell microbubbles at low acoustic pressure amplitudes," *Ultrasonics, Ferroelectrics and Frequency Control, IEEE Transactions on*, vol. 57, no. 8, pp. 1762–1771, 2010.
- [51] K. Cheung, O. Couture, P. D. Bevan, E. Chérin, R. Williams, P. N. Burns, and F. S. Foster, "In vitro characterization of the subharmonic ultrasound signal from definity microbubbles at high frequencies," *Physics in Medicine and Biology*, vol. 53, no. 5, pp. 1209–1223, 2008.
- [52] D. M. J. Cowell, P. R. Smith, and S. Freear, "Phase-inversion-based selective harmonic elimination (PI-SHE) in multi-level switched-mode tone- and frequency- modulated excitation," *Ultrasonics, Ferroelectrics and Frequency Control, IEEE Transactions on*, vol. 60, no. 6, pp. 1084–1097, 2013.
- [53] C. Shen and P. Li, "Harmonic leakage and image quality degradation in tissue harmonic imaging," *Ultrasonics, Ferroelectrics and Frequency Control, IEEE Transactions on*, vol. 48, no. 3, pp. 728–736, 2001.



Sevan Harput received the B.Sc. degree in Microelectronics Engineering and the M.Sc. in Electronic Engineering and Computer Sciences from Sabanci University, Turkey in 2005 and 2007, respectively. He received the Ph.D. degree in 2012 from the University of Leeds. He worked as a teaching and research fellow in Sabanci University between 2007 and 2008. In 2009, he joined to the Ultrasound Group in the School of Electronic and Electrical Engineering, University of Leeds. Currently, he is working as a research fellow in the University of Leeds and he is an administrative assistant in the IEEE Transactions on Ultrasonics, Ferroelectrics and Frequency Control. His research interests include ultrasound medical imaging, coded excitation, nonlinear acoustics and ultrasound contrast agents.



Muhammad Arif Muhammad Arif received his B.S. degree in Biomedical Engineering from Sir Syed University of Engineering & Technology, Karachi, Pakistan, in 2002 and the M.Eng. degree in Telecommunication & Control Engineering from Mehran University of Engineering & Technology, Jamshoro, Pakistan in 2006. In 2007, Mehran University sponsored him to pursue his PhD degree in Biomedical Engineering under the supervision of Dr. Steven Freear. He received his PhD degree from University of Leeds, Leeds United Kingdom, in July 2011. His research interests primarily lie in the area of nonlinear ultrasound imaging. During his doctoral work, Muhammad has investigated the fractional Fourier transform for second harmonic pulse compression and superharmonic imaging using chirp coded excitation. Coded excitation techniques have also been investigated to measure the nonlinear response from contrast microbubbles. Current work seeks to evaluate the performance of nonlinear frequency modulated signals in ultrasound harmonic imaging. He is an Assistant Professor at the Department of Biomedical Engineering at the Mehran University of Engineering & Technology, Jamshoro, Pakistan.



James McLaughlan received his M.Phys. degree in Physics from the University of Bath in 2004, and gained his PhD in 2008 working on the optimisation of high intensity focused ultrasound therapy with cavitation at the Institute of Cancer Research. Subsequently, he moved to Boston University as a post-doctoral research associate where he investigated the use of optical contrast agents exposed to light and sound for the nucleation of cavitation for imaging and therapeutic applications. In 2010 he joined the Ultrasound Group within the School of Electronic and Electrical Engineering at the University of Leeds where he is part of a multidisciplinary team working on engineering therapeutic microbubbles for colorectal cancer treatment. Within the same group he is about to start as an early career research fellow studying the use of nanoparticles for breast cancer imaging and therapy.



David Cowell gained his doctorate from the School of Electronic and Electrical Engineering at the University of Leeds in 2008 working with the Ultrasound Group. His doctoral research area was advanced coding excitation techniques and excitation circuit design for industrial instrumentation and medical imaging systems. During this time he has performed extensive consultancy in instrumentation, FPGA and high-speed digital hardware design. After working as a research consultant in measurement and instrumentation, he joined the Ultrasound Group as a Research Fellow. His main research is currently focused on non-invasive industrial ultrasound measurement. His other active research areas include advanced miniaturized ultrasound excitation systems with low harmonic distortion for phased array imaging, ultrasound system design and signal processing.



Steven Freear (S'95, M'97, SM'11) gained his doctorate in 1997 and subsequently worked in the electronics industry for 7 years as a medical ultrasonic system designer. He was appointed Lecturer (Assistant Professor) and then Senior Lecturer (Associate Professor) in 2006 and 2008 respectively at the School of Electronic and Electrical Engineering at the University of Leeds. In 2006 he formed the Ultrasound Group specializing in both industrial and biomedical research. His main research interest is concerned with advanced analogue and digital signal processing and instrumentation for ultrasonic systems. He teaches digital signal processing, VLSI and embedded systems design, and hardware description languages at both undergraduate and postgraduate level. He has been Associate Editor for IEEE Transactions on Ultrasonics, Ferroelectrics and Frequency Control since 2009, and was appointed Editor-In-Chief in 2013.